Theoretical model of chirality-induced helical self-propulsion

Takaki Yamamoto[1,*] and Masaki Sano[2,†]

[1]*Laboratory for Physical Biology, RIKEN Quantitative Biology Center, Kobe 650-0047, Japan*
[2]*Department of Physics, The University of Tokyo, 7-3-1 Hongo, Bunkyo-ku, Tokyo 113-0033, Japan*

We recently reported the experimental realization of a chiral artificial microswimmer exhibiting helical self-propulsion [T. Yamamoto and M. Sano, Soft Matter **13**, 3328 (2017)]. In the experiment, cholesteric liquid crystal (CLC) droplets dispersed in surfactant solutions swam spontaneously, driven by the Marangoni flow, in helical paths whose handedness is determined by the chirality of the component molecules of CLC. To study the mechanism of the emergence of the helical self-propelled motion, we propose a phenomenological model of the self-propelled helical motion of the CLC droplets. Our model is constructed by symmetry argument in chiral systems, and it describes the dynamics of CLC droplets with coupled time-evolution equations in terms of a velocity, an angular velocity, and a tensor variable representing the symmetry of the helical director field of the droplet. We found that helical motions as well as other chiral motions appear in our model. By investigating bifurcation behaviors between each chiral motion, we found that the chiral coupling terms between the velocity and the angular velocity, the structural anisotropy of the CLC droplet, and the nonlinearity of model equations play a crucial role in the emergence of the helical motion of the CLC droplet.

I. INTRODUCTION

Chirality is an essential aspect of organisms since biomolecules such as DNA, amino acids, and proteins that serve as building blocks are chiral. Living microswimmers, which swim spontaneously in fluid media without an external field in microscale, often exhibit chiral motions, such as rotational [1,2], circular [3,4], and helical [5,6] motions, due to the chiral shapes and motions of the force-generating machineries such as flagella and cilia. For instance, a sperm cell of a sea urchin controls its flagellum in a chiral manner to steer in a circular and a helical path [5,6]. Such chiral dynamics of microswimmers is receiving much attention within the field of active matter physics [7–10].

The chiral motions of microswimmers have also been studied in artificial experimental systems. For instance, in two dimensions, an L-shaped, self-propelled particle exhibits circular motion owing to the chirality of the L shape [9]. We recently reported the first example of chirality-induced helical motion in chiral artificial microswimmers in three dimensions [11], where droplets of cholesteric liquid crystal (CLC), a chiral phase of liquid crystal, swim in helical paths in surfactant solutions. The experimental system of CLC droplets is an ideal three-dimensional (3D) model system for chiral microswimmers, since the strength of both chirality and self-propulsion can be experimentally controlled by altering the concentration of chiral molecules (chiral dopants) in CLC and the surfactant solution. However, the mechanism of the 3D helical motion of CLC droplets is not yet understood.

In this paper, we propose a mathematical model of the chirality-induced helical motion of CLC droplets. In our experimental system [11], when the CLC was injected as microsized droplets in aqueous surfactant solutions, we observed helical motions of the CLC droplets with uniform helical director fields inside the droplets (summarized in Fig. 1). The underlying self-propulsion mechanism is the same as that of the swimming nematic liquid crystal (NLC) droplet in surfactant solution [12–14]; the Marangoni flow induced spontaneously by the dissolution of NLC molecules in surrounding surfactant solutions allows the NLC droplets to move around without any external fields due to the spontaneous symmetry breaking (SSB). By confirming that the helicity of the motion of CLC droplets was determined by the chirality of dopants, we concluded that the helical motion is induced by the chirality. Another remarkable observation was that the helical axis of the droplet precesses around the helical axis of the helical path [see Fig. 1(a)]. This observation means that the helical director field of the droplet and the helical motion are coupled. Consequently, we concluded that the CLC droplets exhibit helical motion as a result of the chiral coupling between the rotation and the Marangoni flow inducing the translation via the helical director field of CLC droplets [see Fig. 1(d)].

Based on the experimental results above, we constructed a simplified model of the swimming CLC droplet by symmetry argument. We applied the model for self-propulsion of the droplets without intrinsic polarity, for which SSB is essential, in contrast to the propulsion of polar self-propelled particles such as asymmetric colloidal particles [15–17]. Tarama and Ohta proposed a model for such a system [18,19], where the dynamics of the particle obeys a coupled time-evolution equation, written in terms of velocity, angular velocity, and a tensor variable representing the geometry of the particle. By introducing coupling terms between the velocity and angular velocity allowed only in chiral systems into their model, we constructed a model for chiral self-propelled droplets.

*takaki.yamamoto@riken.jp
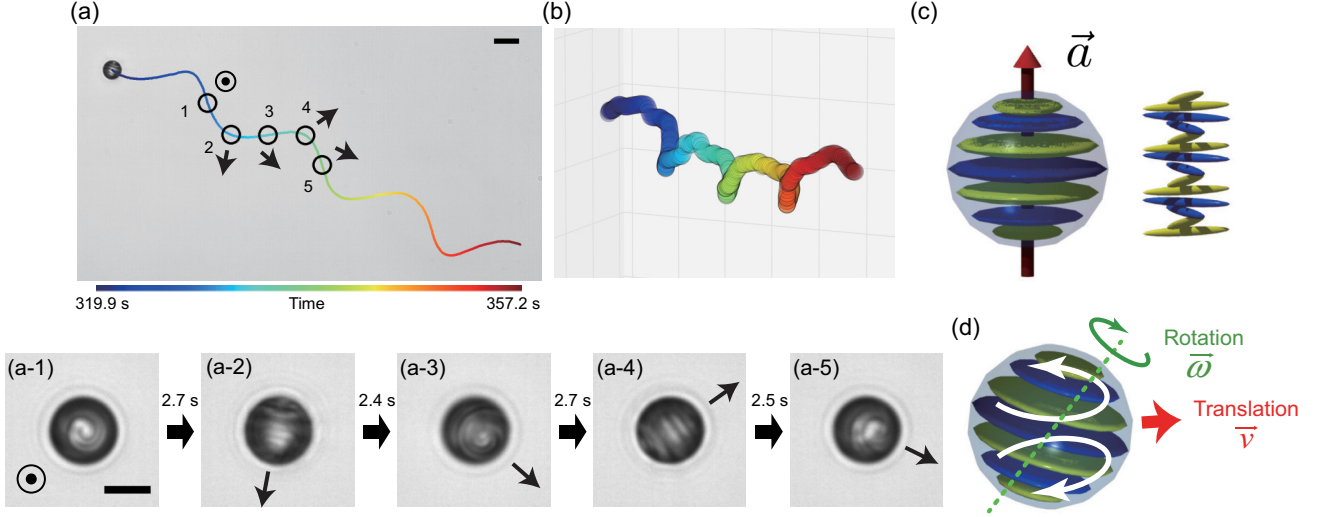†sano@daisy.phys.s.u-tokyo.ac.jp

FIG. 1. Summary of chirality-induced helical motion of a CLC droplet, as reported in Ref. [11]. Reproduced from Ref. [11] with permission from the Royal Society of Chemistry. See Ref. [11] for the detail. (a) A helical trajectory of a CLC droplet projected on a two-dimensional plane is shown. The arrows indicate the direction of the helical axis of the director field of the CLC droplet, as enlarged in panels (a-1)–(a-5). Panels (a-1)–(a-5) correspond to the droplet indicated by the circles numbered 1–5 in (a), respectively. (b) The 3D helical trajectory of the droplet is shown. (c) Schematic image of a CLC droplet with uniform helical director field. Spheroids represent CLC molecules. The red arrow indicates the helical axis a of the CLC droplet. The scale bars are 10 μm in panels (a) and (a-1)–(a-5). (d) Schematic image of the mechanism of helical self-propulsion. The Marangoni flow and the translational motion are represented as the white curved arrows in the CLC droplet and the red arrow, respectively. The green dotted line and curved arrow represent the rotational axis and the rotation, respectively.

Since our model is constructed systematically by symmetry argument, our model should be applicable not only for the self-propulsion of CLC droplets, but also for other chiral self-propelled objects.

II. MODEL DESCRIPTION

We describe the dynamics of a CLC droplet by the coupled Eqs. (1)–(3) in terms of a velocity $\boldsymbol{v}$, an angular velocity $\boldsymbol{\omega}$, and a second rank traceless symmetric tensor Q_{ij} representing the helical director field inside the droplet. Our model does not explicitly contain the surfactant concentration field, which induces the Marangoni flow. Such a reduced model was recently derived in the self-propulsion of the isotropic self-propelled droplet driven by the Marangoni flow by eliminating the degrees of freedom of the concentration field [20,21]:

$$\frac{dv_i}{dt} = \underbrace{\gamma v_i - v_j v_j v_i}_{\text{Self-propulsion or damping}} + \underbrace{a_1 Q_{ij} v_j + a_2 \epsilon_{ijk}\omega_j v_k}_{\text{Rotation}}$$

$$\underbrace{+ \mu^{\text{iso}}\omega_i + \mu Q_{ij}\omega_j}_{\text{Chiral coupling}}, \tag{1}$$

$$\frac{d\omega_i}{dt} = \underbrace{\zeta\omega_i - \omega_j\omega_j\omega_i}_{\text{Self-spinning or damping}} + \underbrace{b_1 Q_{ij}\omega_j}_{} + \underbrace{b_2 \epsilon_{ijk} Q_{jl}v_l v_k}_{\text{Force dipole}}$$

$$\underbrace{+ \nu^{\text{iso}}v_i + \nu Q_{ij}v_j}_{\text{Chiral coupling}}, \tag{2}$$

$$\frac{dQ_{ij}}{dt} = \underbrace{\epsilon_{kjl} Q_{ik}\omega_l - \epsilon_{ikl}\omega_l Q_{kj}}_{\text{Rotation}}. \tag{3}$$

In Eqs. (1)–(3) we define $Q_{ij} = S/2(3a_i a_j - \delta_{ij}) + P/2(b_i b_j - c_i c_j)$ to describe the global symmetry of a whole CLC droplet with a homogeneous helical director field, as we observed in our experiments. a, b, and c are unit vectors. The subscripts $i,j,k,l = 1,2,3$ denote Cartesian components of the tensors. The primary axis a represents the direction of the helical axis of the director field [Fig. 1(c)]. Note that the CLC molecules themselves align perpendicularly to a. Hence, the meaning of Q_{ij} in our model is different from that of the tensor order parameter defined in the NLC [22,23]. We used the second rank tensor Q_{ij} instead of directly using the vector a to represent the helical axis of the droplet because a and $-a$ are equivalent in the case of homogeneous helical director field. We may also consider a biaxial parameter P and the secondary axes b and c ($a \perp b, b \perp c$), since, if we look at the plane crossing the center of the droplet and perpendicular to a, CLC molecules align in a certain preferred direction. In the definition of Q_{ij}, S, and P represent the degrees of anisotropy of the CLC droplet. In this paper, we investigate the behavior of our model by setting $S = 1$ and changing the value of P.

Using Q_{ij} defined above, we constructed the time-evolution Eqs. (1)–(3) by considering the possible terms in a chiral system and keeping some relevant terms. Here we follow the Einstein summation convention and ϵ_{ijk} is a Levi-Civita symbol. The model equations are required to satisfy parity symmetry; they have to be invariant under a parity transformation $P : (x,y,z) \to (-x,-y,-z)$. Under the parity transformation, the components of the velocity $\boldsymbol{v}$, angular velocity $\boldsymbol{\omega}$, and symmetry tensor Q_{ij} of a CLC droplet are transformed as $v_i \to -v_i$, $\omega_i \to \omega_i$, and $Q_{ij} \to Q_{ij}$, respectively. Also, the components of a Levi-Civita symbol ϵ_{ijk} are invariant under the transformation. The most important point is that, in chiral systems, we can introduce terms with pseudoscalar coefficients,

which change the signs under a parity transformation and thus are not allowed in achiral systems [24]. In Eqs. (1)–(3), the coefficients μ^{iso}, μ, ν^{iso}, ν are pseudoscalars allowed only in chiral systems, while γ, ζ, a_1, a_2, b_1, b_2, are scalars allowed even in achiral systems. We certainly find that Eqs. (1)–(3) satisfy parity symmetry.

The meaning of each term with scalar coefficients in Eqs. (1)–(3) is as follows: The first term on the right-hand side of Eqs. (1) and (2) represents the self-propulsion or damping in translation and the self-spinning or damping in rotation, respectively. The second term on the right-hand side of Eqs. (1) and (2) represents nonlinear saturation. If γ or ζ is positive, the droplet has an injection of the energy, resulting in the self-propelled dynamics [18,19,25]; otherwise, the terms mean a damping force and torque. We consider that $\gamma > 0, \zeta < 0$ in our experiments, since the dynamics of the droplet is triggered by the gradient of the surface tension, which results in the Marangoni flow and then translational self-propulsion. In general, the self-spinning may exist in some systems. For instance, a water droplet on silicon oil rotates spontaneously when vibrated vertically [26]. In such a case, ζ should be positive. The terms with the coefficients a_1 and b_1 represent the anisotropy of self-propulsion or damping. The signs of the coefficients determine the easy axis of the translation or rotation. If the coefficients are positive, $\boldsymbol{a}$ is the easy axis. Otherwise, any direction perpendicular to $\boldsymbol{a}$ is the preferred direction in an uniaxial case, and an eigenvector corresponding to the minimum eigenvalue of Q_{ij} is the preferred direction in biaxial cases. The terms with a_2 and b_2 are the lowest order terms describing the achiral coupling between $\boldsymbol{v}$ and $\boldsymbol{\omega}$ in each time-evolution equation. The term with a_2 means the turning of the translational direction due to the rotation; a_2 should approach 1 from 0, as the coupling between $\boldsymbol{v}$ and $\boldsymbol{\omega}$ gets stronger. We later discuss the term with b_2 in detail.

The most essential part of our model is the coupling terms with pseudoscalar coefficients μ^{iso}, μ, ν^{iso}, ν, which represent the chiral coupling between the translation induced by the Marangoni flow and the rotation through the helical director field of the CLC droplet. Since these terms are the off-diagonal couplings in the linear nonequilibrium thermodynamics [24], we expect a reciprocal relation and hence assume that $\mu^{\text{iso}} = \nu^{\text{iso}}$ and $\mu = \nu$.

Numerical simulations were performed based on Eqs. (1)–(3) by the fourth-order Runge-Kutta method ($\Delta t = 1.0 \times 10^{-4}$). The initial conditions for velocity $\boldsymbol{v}$ and angular velocity $\boldsymbol{\omega}$ were provided by a Gaussian distribution with a mean of zero (standard deviation $\sigma = 0.5$). We investigate the dynamics by changing the strength of the self-propulsion γ, the chiral couplings μ^{iso}, μ, ν^{iso}, ν, and b_2. For simplicity, we control the strength of chiral couplings with a pseudoscalar parameter μ by setting $\mu = \nu$, $\mu^{\text{iso}} = \nu^{\text{iso}} = 0.7\mu$. The other parameters are fixed as $a_1 = -1$, $a_2 = 0.9$, $\zeta = -3$, $b_1 = 0$, $b_2 = 0.4$, unless otherwise noted. Here a_1 is set as negative for the following reason. It is reported that the effective viscosity in the direction of the helical axis is comparably higher than that of perpendicular to the helical axis [27]. Hence, the Marangoni flow, which induces the translation, is likely to occur perpendicularly to the helical axis to minimize the dissipation. Here a_2 is set to be smaller than 1, since the surfactant concentration field, which is the origin of the translation $\boldsymbol{v}$,
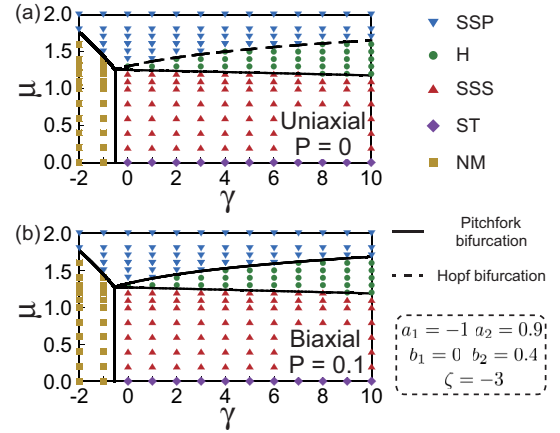

FIG. 2. Phase diagrams (a) in the uniaxial ($P = 0$) and (b) biaxial case ($P = 0.1$), respectively [square: NM (no motion), upward triangle: SSS (spinning straight motion along secondary axis), downward triangle: SSP (spinning straight motion along primary axis), diamond: ST (straight motion) and circle: H (helical motion)]. The lines indicate linear stability limits of NM, SSS, and SSP (solid line: pitchfork bifurcation, dashed line: Hopf bifurcation).

should not fully follow the rotation $\boldsymbol{\omega}$. In addition, we consider isotropic damping of rotational motion ($\zeta < 0, b_1 = 0$), since the droplet is spherical. Furthermore, we examine the effects of the uniaxiality and the biaxiality by setting $P = 0$ or $P = 0.1$.

III. RESULTS AND DISCUSSION

A. Phase diagram

Figure 2 shows the phase diagrams obtained by numerical simulations and linear stability analysis of Eqs. (1)–(3) in both the uniaxial and biaxial case. We numerically obtained five phases: No Motion (NM), Straight motion (ST), Spinning Straight motion (SS) along Secondary axis (SSS) and SS along Primary axis (SSP), and Helical motion (H). In NM phase, the droplet is motionless. In ST phase, the droplet moves perpendicularly to $\boldsymbol{a}$ without any rotation, which is observed in the limit of $\mu = 0$. SS is a phase where the droplet moves with $\boldsymbol{v} \parallel \boldsymbol{\omega}$. SS can be classified into two phases: SSS and SSP, where $\boldsymbol{v}$ is perpendicular and parallel to $\boldsymbol{a}$, respectively (see Fig. 3). When neither $\boldsymbol{v} \parallel \boldsymbol{\omega}$ nor $\boldsymbol{v} \perp \boldsymbol{\omega}$, we classify the motion into H phase. In H phase, the helix was right-handed when $\mu > 0$. Importantly, changing the sign of μ—inversion of the chirality—provided a mirror image of the dynamics, consistent with our experiments in Ref. [11].
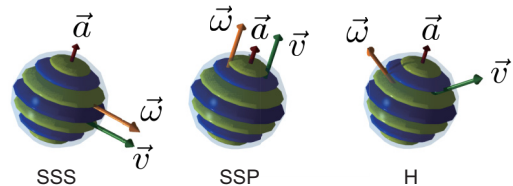

FIG. 3. Schematic images of SSS (spinning straight motion along secondary axis), SSP (spinning straight motion along primary axis), and H (helical motion), respectively. Each arrow represents $\boldsymbol{a}, \boldsymbol{v}$, and $\boldsymbol{\omega}$.
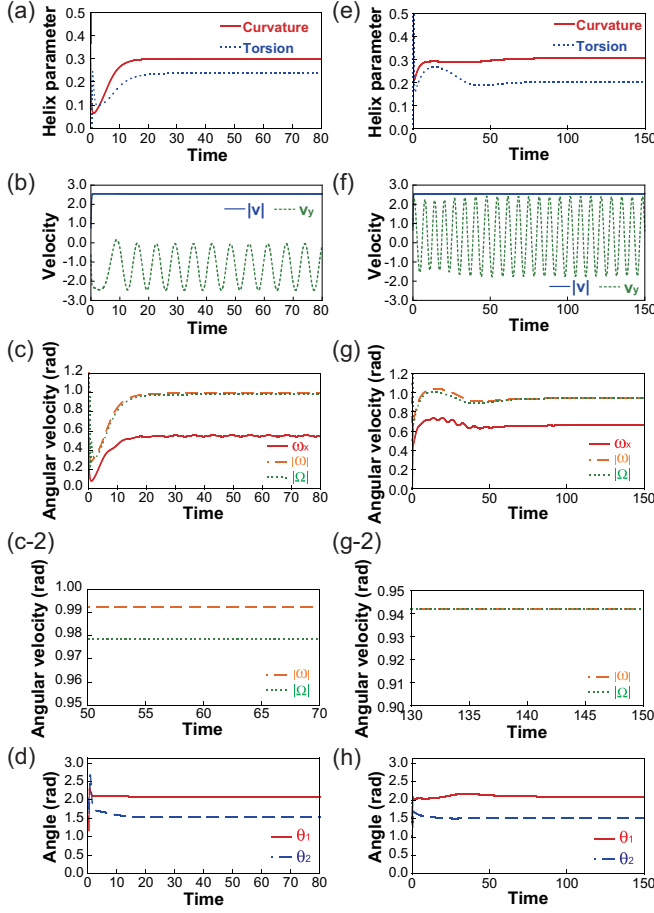
FIG. 4. Time evolution of (a) curvature κ and torsion τ, (b) a component of $\boldsymbol{v}$ and absolute value of velocity $\boldsymbol{v}$, (c) a component of $\boldsymbol{\omega}$, absolute values of $\boldsymbol{\omega}$ and $\boldsymbol{\Omega}$, and (d) θ_1 and θ_2 in a helical motion ($P = 0, b_2 = 0.4, \gamma = 6, \mu = 1.4$). The same properties for a helical motion in a biaxial case ($P = 0.1, b_2 = 0.4, \gamma = 6, \mu = 1.4$) are shown in (e)–(h). The enlarged time series of $|\boldsymbol{\omega}|$ and $|\boldsymbol{\Omega}|$ are shown in (c-2) and (g-2) for uniaxial and biaxial cases, respectively.

In Figs. 2(a) and 2(b), the lines indicate the linear stability limits of the NM, SSS, and SSP phases, consistent with the numerical results. We show the details of the bifurcation analysis in Appendix B. In the uniaxial case where $P = 0$, pitchfork bifurcations occur at the NM-SSS, NM-SSP, and SSS-H boundaries, whereas the Hopf bifurcation occurs at the SSP-H boundary. The Hopf bifurcation at the SSP-H boundary in the uniaxial case is probably related to the rotational symmetry around $\boldsymbol{a} \parallel \boldsymbol{v} \parallel \boldsymbol{\omega}$ in SSP. In contrast, this rotational symmetry is broken in biaxial cases. As a result, we did not observe the Hopf bifurcation at the SSP-H boundary in the biaxial case ($P = 0.1$).

B. Dynamics

In our model, whether the droplet is uniaxial or biaxial also plays a key role in the dynamics of helical motion. Figure 4 shows the time evolution of several essential variables in helical trajectories for uniaxial and biaxial cases which identify the helical motion. In both the uniaxial case ($P = 0$) and the biaxial case ($P = 0.1$), we numerically found that the helical
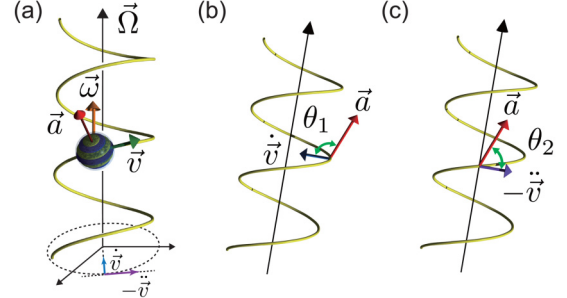

FIG. 5. Definition of each vector characterizing the property of helical motion is schematically drawn for a perfect helical trajectory. (a) The direction of helical axis $\boldsymbol{a}$, velocity $\boldsymbol{v}$, angular velocity $\boldsymbol{\omega}$ of a CLC droplet, and angular velocity $\boldsymbol{\Omega}$ of the helical motion are shown. The dotted circle represents the projection of the helical trajectory (yellow curve) on the plane perpendicular to $\boldsymbol{\Omega}$. (b, c) Definitions of θ_1 and θ_2 are shown.

path is a perfect helix; that is, the curvature κ and torsion τ of the path are time-independent in the steady state as shown in Fig. 4(a) for a uniaxial case and Fig. 4(e) for a biaxial case. $|\boldsymbol{v}|$ and $|\boldsymbol{\omega}|$ are also time-independent [Figs. 4(b), 4(c), 4(f), and 4(g)].

In contrast, the details of rotational motion are different in both cases. We define the angular velocity of the helical motion as $\boldsymbol{\Omega} = \Omega \boldsymbol{e}_q$, where Ω is the absolute value of the angular velocity, and $\boldsymbol{e}_q$ is a unit vector parallel to the direction of the helical axis of the trajectory. As shown in Fig. 5(a), $\dot{\boldsymbol{v}}/|\dot{\boldsymbol{v}}|$ and $\ddot{\boldsymbol{v}}/|\ddot{\boldsymbol{v}}|$ are, respectively, the radius and tangential unit vectors of the circular trajectory which is a projection of the helical trajectory on the plane perpendicular to the helical axis, when the trajectory is a perfect helix and $|\boldsymbol{v}|$ is time-independent like in our cases. Hence, $\boldsymbol{e}_q$ is defined as $\boldsymbol{e}_q = (\dot{\boldsymbol{v}}/|\dot{\boldsymbol{v}}|) \times (\ddot{\boldsymbol{v}}/|\ddot{\boldsymbol{v}}|)$. In order to identify the geometrical relationship between the direction of the helical axis $\boldsymbol{e}_q$ of the trajectory and the helical axis $\boldsymbol{a}$ of the droplet, we introduce the angle θ_1 and θ_2, which are defined as $\theta_1 = \arccos(\dot{\boldsymbol{v}} \cdot \boldsymbol{a}/|\dot{\boldsymbol{v}}|)$ and $\theta_2 = \arccos(-\ddot{\boldsymbol{v}} \cdot \boldsymbol{a}/|\ddot{\boldsymbol{v}}|)$. θ_1 and θ_2 are depicted schematically in Figs. 5(b) and 5(c), respectively. Figures 4(g) and 4(g-2) show that, in the biaxial case, $|\boldsymbol{\omega}|$ is identical to $|\boldsymbol{\Omega}|$ and the components of $\boldsymbol{\omega}$ are time-independent (we show one of the components). In contrast, Figs. 4(c) and 4(c-2) show that, in the uniaxial case, oscillation of the components of $\boldsymbol{\omega}$ and deviation of $|\boldsymbol{\omega}|$ from $|\boldsymbol{\Omega}|$ are observed. θ_1 and θ_2 were time-independent for both cases in the steady states [Figs. 4(d) and 4(h)]. Hence, we find that, in the uniaxial case, an additional spinning motion around the helical axis $\boldsymbol{a}$ of the CLC droplet occurs during the helical motion. The oscillation should be originating from a limit cycle in H phase, consistent with the Hopf bifurcation in the uniaxial case. This insight into the uniaxial limit $P = 0$ will be important, since the biaxiality of the CLC droplet should decrease until it vanishes as the wave number of the helical director field gets larger.

C. Force dipole represented by term with b_2

Here we discuss the term with b_2. As the arrows in Fig. 1(a) indicate, we find that the helical axis of the droplet is directed towards the outside from the helical axis of the helical path.
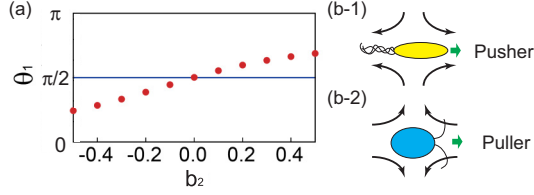
FIG. 6. (a) Relation between θ_1 and b_2 in the uniaxial case ($\gamma = 6, \mu = 1.4$). The solid line represents $\theta_1 = \pi/2$. (b-1) and (b-2) Flow fields around a pusher-type and a puller-type microswimmer are shown by the curved arrows. *Escherichia coli* and *Chlamydomonas reinhardtii* are used as an example of each type of microswimmer, respectively.

To quantify this feature, we use $\theta_1 = \arccos(\dot{\boldsymbol{v}} \cdot \boldsymbol{a}/|\dot{\boldsymbol{v}}|)$ [see Fig. 5(b)]. When $\boldsymbol{a}$ is directed outside like in the experimental result, $\theta_1 > \pi/2$. The effect of b_2 on θ_1 is numerically investigated in Fig. 6(a), which suggests that θ_1 is larger than $\pi/2$ when $b_2 > 0$. Accordingly, our model predicts that $b_2 > 0$ in the CLC droplet experiment. Meanwhile, the second-rank symmetric tensor $v_i v_j$ in the term with b_2 represents the symmetry of the flow field generated by the force dipole, by which the droplet is classified into a pusher- or a puller-type microswimmer in the squirmer model [28,29]. We schematically depict such flow fields in Fig. 6(b). For example, since *Escherichia coli* pushes the surrounding fluid forwards and backwards while swimming, it is classified as a pusher [30,31]. In contrast, *Chlamydomonas reinhardtii* pulls surrounding fluid along the center line of the body, and hence it is called a puller [31,32]. This term with b_2 is derived from the torque on the helical director field due to a force dipole. We can determine the sign of b_2 if we know whether the CLC droplet is a pusher or a puller, as well as how the force dipole induces the torque on the CLC droplet. Further investigation into the flow field and the response of the CLC droplet in it is required to elucidate the term with b_2. Nevertheless, our model certainly shows the importance of the force dipole in CLC droplet dynamics.

D. Effects of the structural anisotropy of a particle and the nonlinearity on the phase behavior

We found that our model exhibits several chiral motions—SSS, SSP, and H—depending on the parameters γ and μ for self-propulsion and chiral couplings (Fig. 2). Here we discuss the mechanism of the emergence of the H phase in our model. We suspected that the helical motion appears owing to either one or both of the structural anisotropy of a particle, represented by the second-rank tensor Q_{ij} and the nonlinearity in our model. In our model, we have four nonlinear terms with respect to $\boldsymbol{v}$ and $\boldsymbol{\omega}$: $v_j v_j v_i$, $a_2 \epsilon_{ijk} \omega_j v_k$, $\omega_j \omega_j \omega_i$, and $b_2 \epsilon_{ijk} Q_{jl} v_l v_k$. Note that the term with a_2 brings nonlinearity to our models when $a_2 \neq 1$, since if we look at our equations with the particle frame introduced in Appendix A, $(a_2 - 1)$ is a coefficient which brings nonlinearity into the equations [see Eq. (A7) in Appendix A]. We investigated the effects of the particle anisotropy and the nonlinearity on the model behavior by eliminating (1) both the particle anisotropy and the nonlinearity, (2) only particle anisotropy, and (3) only nonlinearity, as follows.
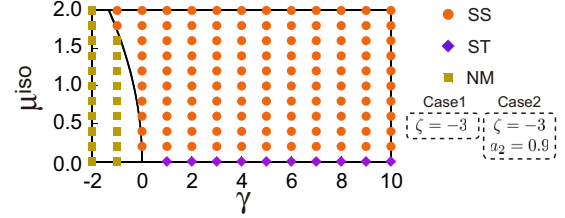

FIG. 7. Phase diagram of our model without particle structural anisotropy represented by a second-rank tensor Q_{ij} (cases 1 and 2 in the main text). Since the phase diagrams for cases 1 and 2 are the same, a single phase diagram is shown.

In case 1, we performed numerical simulations with Eqs. (4) and (5) by eliminating the terms including Q_{ij} and the nonlinear terms $\omega_j \omega_j \omega_i, b_2 \epsilon_{ijk} Q_{jl} v_l v_k$ from Eqs. (1)–(3) and setting $a_2 = 1$. We kept the nonlinear term $v_j v_j v_i$, since it is essential for the self-propulsion of the droplet. Note that the time evolution equation of Q_{ij} is unnecessary in cases 1 and 2, since we are considering isotropic chiral self-propelled particles:

$$\frac{dv_i}{dt} = \underbrace{\gamma v_i - v_j v_j v_i}_{\text{Self}-\text{propulsion or damping}} + \underbrace{\epsilon_{ijk} \omega_j v_k}_{\text{Rotation}} + \underbrace{\mu^{\text{iso}} \omega_i}_{\text{Chiral coupling}},$$

(4)

$$\frac{d\omega_i}{dt} = \underbrace{\zeta \omega_i}_{\text{Damping}} + \underbrace{\nu^{\text{iso}} v_i}_{\text{Chiral coupling}}.$$

(5)

Figure 7 shows the phase diagram. Since we eliminated the terms with μ and ν here, we controlled the chirality of our system by changing μ^{iso} and ν^{iso}. Here we again assumed a reciprocal relation $\mu^{\text{iso}} = \nu^{\text{iso}}$; ζ is also set to the same value as that used in Fig. 2 ($\zeta = -3$). We found that the model does not exhibit helical motions, but only NM, ST, and SS. Here SS is not classified into SSS or SSP since we eliminated the particle anisotropy Q_{ij}. The linear stability limit of NM is shown as a curve $\mu^{\text{iso}} = \sqrt{\zeta \gamma}$ in Fig. 7. We also confirmed that SS is linearly stable in this case. In Eqs. (4) and (5), the isotropic chiral coupling terms $\mu^{\text{iso}} \omega_i$ and $\nu^{\text{iso}} v_i$ tend to align $\boldsymbol{v}$ and $\boldsymbol{\omega}$ in the parallel direction. Since there is no term which potentially disturbs this condition $\boldsymbol{v} \parallel \boldsymbol{\omega}$, we do not observe helical motions in case 1.

In case 2, we added two nonlinear terms $\omega_j \omega_j \omega_i$ and $a_2 \epsilon_{ijk} \omega_j v_k (a_2 \neq 1)$ into Eqs. (4) and (5) and obtained Eqs. (6) and (7). In the numerical simulation of Eqs. (6) and (7), a_2 and ζ are set to the same values as that used in Fig. 2 ($a_2 = 0.9$ and $\zeta = -3$). We found that the phase diagram and linear stability limit of NM in case 2 are the exact same as that of case 1. Hence, isotropic chiral self-propelled particles considered here do not exhibit helical motion even when we introduce nonlinear terms into our model. The structural anisotropy of the particle is necessary for helical self-propulsion. We consider that SS phase is stable also in case 2, since $\omega_j \omega_j \omega_i$ only effectively reduces the damping constant ζ in Eq. (7), and $\boldsymbol{\omega}$ still tends to
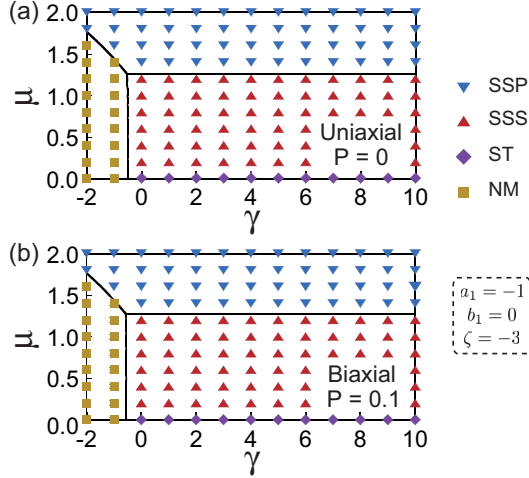
FIG. 8. Phase diagrams of our model without nonlinear terms except for the self-propulsion term, for (a) the uniaxial ($P = 0$) and (b) the biaxial case ($P = 0.1$). The other coefficients in linear terms are the same as those we applied in the nonlinear cases in Fig. 2. The phase boundaries between SSS and SSP are parallel to the horizontal axes.

align in the direction parallel to v:

$$\frac{dv_i}{dt} = \underbrace{\gamma v_i - v_j v_j v_i}_{Self-propulsion\ or\ damping} + \underbrace{a_2 \epsilon_{ijk} \omega_j v_k}_{Rotation} + \underbrace{\mu^{iso} \omega_i}_{Chiral\ coupling},$$

(6)

$$\frac{d\omega_i}{dt} = \underbrace{\zeta \omega_i - \omega_j \omega_j \omega_i}_{Self-spinning\ or\ damping} + \underbrace{\nu^{iso} v_i}_{Chiral\ coupling}.$$

(7)

To investigate case 3, we eliminated the terms $\omega_j \omega_j \omega_i$ and $b_2 \epsilon_{ijk} Q_{jl} v_l v_k$ from Eqs. (1)–(3) and set $a_2 = 1$. Hence, the model equations for case 3 are as follows:

$$\frac{dv_i}{dt} = \underbrace{\gamma v_i - v_j v_j v_i + a_1 Q_{ij} v_j}_{Self-propulsion\ or\ damping} + \underbrace{\epsilon_{ijk} \omega_j v_k}_{Rotation}$$

$$+ \underbrace{\mu^{iso} \omega_i + \mu Q_{ij} \omega_j}_{Chiral\ coupling},$$

(8)

$$\frac{d\omega_i}{dt} = \underbrace{\zeta \omega_i + b_1 Q_{ij} \omega_j}_{Damping} + \underbrace{\nu^{iso} v_i + \nu Q_{ij} v_j}_{Chiral\ coupling},$$

(9)

$$\frac{dQ_{ij}}{dt} = \underbrace{\epsilon_{kjl} Q_{ik} \omega_l - \epsilon_{ikl} \omega_l Q_{kj}}_{Rotation}.$$

(10)

Figure 8 shows the phase diagrams in case 3 for both uniaxial ($P = 0$) and biaxial ($P = 0.1$) cases. Other parameters are the same as those used in Fig. 2. We found that the model does not exhibit helical motions, but only NM, ST, SSS, and SSP. The linear stability limits of NM, SSS, and SSP are also shown as curves in Fig. 8. The linear stability limits of SSS and SSP coincide at the boundary between SSS and SSP, and the boundary between SSS an SSP is parallel to the γ axis. Under the parameters applied in case 3, the easy axis of the translational self-propulsion is perpendicular to the helical axis

a of the droplet, while chiral couplings between v and ω are stronger in the direction parallel to a than in that perpendicular to a. Hence, SSS appears when μ is low and the easy axis of the translational self-propulsion takes priority, while SSP appears when μ is high and chiral couplings are dominant. In our original nonlinear model with Eqs. (1)–(3), since the vector $\epsilon_{ijk} \omega_j v_k$ ($\epsilon_{ijk} Q_{jl} v_l v_k$) is perpendicular to ω (v), the term tends to orient v (ω) perpendicularly to ω (v). Hence, we consider that nonlinear terms $a_2 \epsilon_{ijk} \omega_j v_k$ and $b_2 \epsilon_{ijk} Q_{jl} v_l v_k$ in Eqs. (1)–(3) can break the condition $v \parallel \omega$ satisfied in SSS and SSP, and H phase appears between SSS and SSP phases. Given all these results for cases 1, 2, and 3, both the structural anisotropy Q_{ij} and the nonlinearity are essential for helical self-propulsion in our model.

IV. SUMMARY

In this paper, we proposed a phenomenological model of chirality-induced helical self-propulsion of a CLC droplet based on a theoretical framework of the self-propelled objects [18,19,25]. We found that our model exhibits helical motion owing to the nonlinearity of our model equations and the chiral coupling terms between v and ω. Interestingly, in addition to the helical motion, we found that other chiral motions which we call SSS and SSP appear as solutions of the model equations. Transitions between each chiral motion are associated with the bifurcation of the dynamical system. Although it has been already reported in Refs. [19,33] that the helical motion of the self-propelled droplets can appear with the bifurcation behavior in their models, the left- and right-handed helical trajectories appear with equal probability because the chiral symmetry is not broken in such models. Also, we found that the uniaxiality and biaxiality of the CLC droplet change the type of bifurcation between SSP and H: Hopf bifurcation for uniaxial case ($P = 0$) and pitchfork bifurcation in biaxial case ($P = 0.1$). These features have not been investigated yet in previously reported models which exhibit helical motions [8,19,33–38]. Furthermore, our model sheds light on the importance of the force dipoles on the detail dynamics of helical motions, which classify the microswimmer into a pusher-type or a puller-type.

To justify our model as a model of a CLC droplet, it is necessary to experimentally test the phase diagrams and bifurcations. In principle, we can control the parameters μ and γ by changing the concentration of chiral dopants and surfactant solutions. We also expect that the uniaxiality of the droplet will increase by increasing the chirality of the droplet, since the anisotropy perpendicular to the helical axis will decrease when the pitch of the CLC is short. Furthermore, the measurement of the flow field inside and outside the droplet is also required to justify our model and especially the importance of force dipoles.

To summarize, our model succeeded in predicting nontrivial phase diagrams and bifurcation structures in the dynamics of CLC droplets in surfactant solution. We believe that our model will provide important insights into the role of chirality in dynamics of self-propelled particles because of the generalizability of the formulation of our model equations constructed by the symmetry argument.

APPENDIX A: COORDINATE TRANSFORMATION FROM THE LABORATORY FRAME TO THE PARTICLE FRAME

To simplify the linear stability analysis, a coordinate transformation from the laboratory frame $(\boldsymbol{v}, \boldsymbol{\omega}, \boldsymbol{Q})$ to the particle frame $(\tilde{\boldsymbol{v}}, \tilde{\boldsymbol{\omega}}, \tilde{\boldsymbol{Q}})$ was performed. For simplicity, we rewrite Eqs. (1)–(3) in more general form as follows:

$$\frac{dv_i}{dt} = f_i(\boldsymbol{v}, \boldsymbol{Q}, \boldsymbol{\omega}), \tag{A1}$$

$$\frac{d\omega_i}{dt} = g_i(\boldsymbol{v}, \boldsymbol{Q}, \boldsymbol{\omega}), \tag{A2}$$

$$\frac{dQ_{ij}}{dt} = \epsilon_{kjl} Q_{ik}\omega_l - \epsilon_{ikl}\omega_l Q_{kj}. \tag{A3}$$

Since the particle frame is a rotating reference frame with the angular velocity $\boldsymbol{\omega}$, we have the following time-evolution equations in the particle frame:

$$\frac{d\tilde{v}_i}{dt} = f_i(\tilde{\boldsymbol{v}}, \tilde{\boldsymbol{Q}}, \tilde{\boldsymbol{\omega}}) - \epsilon_{ijk}\tilde{\omega}_j\tilde{v}_k, \tag{A4}$$

$$\frac{d\tilde{\omega}_i}{dt} = g_i(\tilde{\boldsymbol{v}}, \tilde{\boldsymbol{Q}}, \tilde{\boldsymbol{\omega}}), \tag{A5}$$

$$\frac{d\tilde{Q}_{ij}}{dt} = 0. \tag{A6}$$

Note that, if we define a 3×3 orthogonal matrix $\boldsymbol{P}$ as the transformation matrix, where $\tilde{\boldsymbol{v}} = \boldsymbol{P}\boldsymbol{v}, \tilde{\boldsymbol{\omega}} = \boldsymbol{P}\boldsymbol{\omega}, \tilde{\boldsymbol{Q}} = \boldsymbol{P}\boldsymbol{Q}\boldsymbol{P}^T$, we have the relation $\dot{\boldsymbol{P}}(t) = \boldsymbol{\Omega}(t)\boldsymbol{P}(t)$. Here the second rank antisymmetric tensor $\boldsymbol{\Omega}$ is defined as $\Omega_{ij} = \epsilon_{ijk}\omega_k$.

Consequently, we only need to perform the linear stability analysis of the following time-evolution equations with respect to $\tilde{\boldsymbol{v}}$ and $\tilde{\boldsymbol{\omega}}$ in the particle frame:

$$\frac{d\tilde{v}_i}{dt} = \gamma \tilde{v}_i - \tilde{v}_j\tilde{v}_j\tilde{v}_i + a_1\tilde{Q}_{ij}\tilde{v}_j + (a_2 - 1)\epsilon_{ijk}\tilde{\omega}_j\tilde{v}_k$$
$$+ \mu^{\text{iso}}\tilde{\omega}_i + \mu\tilde{Q}_{ij}\tilde{\omega}_j, \tag{A7}$$

$$\frac{d\tilde{\omega}_i}{dt} = \zeta\tilde{\omega}_i - \tilde{\omega}_j\tilde{\omega}_j\tilde{\omega}_i + b_1\tilde{Q}_{ij}\tilde{\omega}_j + b_2\epsilon_{ijk}\tilde{Q}_{jl}\tilde{v}_l\tilde{v}_k$$
$$+ \nu^{\text{iso}}\tilde{v}_i + \nu\tilde{Q}_{ij}\tilde{v}_j. \tag{A8}$$

In the linear stability analysis, we set $\tilde{Q}_{ij}$ as follows:

$$\tilde{Q} = \begin{bmatrix} q_1 = S & 0 & 0 \\ 0 & q_2 = -\frac{1}{2}(S - P) & 0 \\ 0 & 0 & q_3 = -\frac{1}{2}(S + P) \end{bmatrix}. \tag{A9}$$

Here $\boldsymbol{a}, \boldsymbol{b},$ and $\boldsymbol{c}$ in the main text are parallel to x axis, y axis, and z axis in the particle frame, and q_1, q_2, and q_3 are the eigenvalues of Q_{ij}, corresponding to the eigenvectors $\boldsymbol{a}, \boldsymbol{b}$ and $\boldsymbol{c}$. S and P are the uniaxial and biaxial parameters from the main text. We investigated the behavior of our model by setting $S = 1$ and changing the value of P ($P = 0$ or $P = 0.1$).

APPENDIX B: LINEAR STABILITY ANALYSIS

We show the detail of the linear stability analysis of NM (No motion), SSS (Spinning Straight motion along Secondary axis), and SSP (Spinning Straight motion along Primary axis) using the particle frame introduced above. In the following, we take $(\tilde{v}_1, \tilde{v}_2, \tilde{v}_3, \tilde{\omega}_1, \tilde{\omega}_2, \tilde{\omega}_3)$ as our dynamical variables.

1. Linear stability analysis of NM

In NM phase, $\tilde{\boldsymbol{v}} = \tilde{\boldsymbol{\omega}} = \boldsymbol{0}$, which is a trivial fixed point of Eqs. (A7) and (A8). We obtain the Jacobian J_{NM} as follows:

$$J_{\text{NM}} = \begin{bmatrix} \gamma + a_1 q_1 & 0 & 0 & \mu^{\text{iso}} + \mu q_1 & 0 & 0 \\ 0 & \gamma + a_1 q_2 & 0 & 0 & \mu^{\text{iso}} + \mu q_2 & 0 \\ 0 & 0 & \gamma + a_1 q_3 & 0 & 0 & \mu^{\text{iso}} + \mu q_3 \\ \nu^{\text{iso}} + \nu q_1 & 0 & 0 & \zeta + b_1 q_1 & 0 & 0 \\ 0 & \nu^{\text{iso}} + \nu q_2 & 0 & 0 & \zeta + b_1 q_2 & 0 \\ 0 & 0 & \nu^{\text{iso}} + \nu q_3 & 0 & 0 & \zeta + b_1 q_3 \end{bmatrix}. \tag{B1}$$

With respect to the reciprocal relation among pseudoscalar parameters described in the main text, we introduce a parameter α for simplicity as follows:

$$\mu^{\text{iso}} = \left(\tfrac{1}{2} + \alpha\right)\mu, \tag{B2}$$

$$\mu = \nu, \tag{B3}$$

$$\mu^{\text{iso}} = \nu^{\text{iso}}. \tag{B4}$$

Note that we set $\alpha = 0.2$ in the main text. Setting $a_1 = -1$, $b_1 = 0$ as in the main text, we analytically obtain the linear stability limit as follows:

$$\gamma = \begin{cases} 1 + \frac{1}{\zeta}\left(\frac{3}{2} + \alpha\right)^2 \mu^2, & \text{if } \gamma < \frac{-3/4 - P/2 - \alpha - \alpha^2}{3/2 - P/2 + 2\alpha}, \\ -\left(\frac{1}{2} + \frac{P}{2}\right) + \frac{1}{\zeta}\left(\alpha - \frac{P}{2}\right)^2 \mu^2, & \text{otherwise}. \end{cases} \tag{B5}$$

Also, the coordinate of the intersection of the two branches are $(\gamma, \mu) = \left(\frac{-3/4 - P/2 - \alpha - \alpha^2}{3/2 - P/2 + 2\alpha}, \sqrt{\frac{-\zeta}{(2\alpha + 3/2 - P/2)}}\right)$.

Now we investigate the types of bifurcation from NM to SSS and SSP, respectively.

a. Bifurcation from NM to SSS

SSS is the spinning straight motion (SS) along secondary axis. When $a_1 < 0$ as considered in the main text, the axis which has the lowest negative eigenvalue is the favorable direction of the motion in SSS. Hence, in the biaxial case, the spinning straight motion (SS) with $\tilde{v} \parallel \tilde{\omega} \parallel c$ appears as SSS. In contrast, since two secondary axes b and c are degenerate in the uniaxial case, $\tilde{v}$ and $\tilde{\omega}$ in SSS are in the arbitrary direction perpendicular to the primary axis a. Putting the solution $\tilde{v} = (0, 0, \tilde{v}_s)$ and $\tilde{\omega} = (0, 0, \tilde{\omega}_s)$ for SSS in both cases, we obtain the following equations for $(\tilde{v}_s, \tilde{\omega}_s)$:

$$(\mu^{\text{iso}} + q_3\mu)\tilde{\omega}_s = \tilde{v}_s^3 - (\gamma + a_1 q_3)\tilde{v}_s, \tag{B6}$$

$$(\nu^{\text{iso}} + q_3\nu)\tilde{v}_s = \tilde{\omega}_s^3 - (\zeta + b_1 q_3)\tilde{\omega}_s. \tag{B7}$$

In the range of the parameters in the main text, we have three solutions: 0 and two symmetric solutions with respect to the origin of the phase space. In the uniaxial case with the parameters used in the phase diagram in Fig. 2(a), the symmetric solutions are obtained analytically by using Mathematica as follows:

$$\tilde{\omega}_s = A(\mu, \Delta_1), \tag{B8}$$

$$\tilde{v}_s = \frac{1}{\mu}[15A(\mu, \Delta_1) + 5A(\mu, \Delta_1)^3], \tag{B9}$$

where $\Delta_1 > 0$ is defined as $\Delta_1 = \gamma - \{-(1/2 + P/2) + (\alpha - P/2)^2 \mu^2/\zeta\}$ to represent the deviation of γ from the NM-SSS boundary calculated in Eq. (B5), and $A(\mu, \Delta_1)$ is real solutions of the following equation:

$$A^2\{(50\,625 - 75\Delta_1\mu^2 + \mu^4) + 50\,625A^2 + 16\,875A^4 + 1875A^6\} = 225\Delta_1\mu^2. \tag{B10}$$

Considering that the left-hand side of Eq. (B10) is an even function which has a minimum equal to zero at $A = 0$ and a

monotonically increasing function when $A > 0$, Eq. (B10) has only two real solutions with opposite signs which converge continuously to zero in the limit $\Delta_1 = 0$. Hence, we find that the bifurcation from NM to SSS is a pitchfork bifurcation in the uniaxial case. Also in the biaxial case ($P = 0.1$), we found that the bifurcation is a pitchfork bifurcation with the same explanation qualitatively as that for the uniaxial case above.

b. Bifurcation from NM to SSP

In SSP, $\tilde{v}$ is parallel to a and $\tilde{\omega}$ for both uniaxial and biaxial cases. Putting the solution $\tilde{v} = (\tilde{v}_p, 0, 0)$ and $\tilde{\omega} = (\tilde{\omega}_p, 0, 0)$, we obtain the following equations for $(\tilde{v}_p, \tilde{\omega}_p)$:

$$(\mu^{\text{iso}} + q_1\mu)\tilde{\omega}_p = \tilde{v}_p^3 - (\gamma + a_1 q_1)\tilde{v}_p, \tag{B11}$$

$$(\nu^{\text{iso}} + q_1\nu)\tilde{v}_p = \tilde{\omega}_p^3 - (\zeta + b_1 q_1)\tilde{\omega}_p. \tag{B12}$$

In the range of the parameters in the main text, we have three solutions: 0 and two symmetric solutions with respect to the origin of the phase space. With the parameters used in the phase diagram in Figs. 2(a) and 2(b), the symmetric solutions are obtained analytically by using Mathematica as follows:

$$\tilde{\omega}_p = B(\mu, \Delta_2), \tag{B13}$$

$$\tilde{v}_p = \frac{1}{17\mu}[30B(\mu, \Delta_2) + 10B(\mu, \Delta_2)^3], \tag{B14}$$

where $\Delta_2 > 0$ is defined as $\Delta_2 = \gamma - \{1 + (3/2 + \alpha)^2\mu^2/\zeta\}$ to represent the deviation of γ from the NM-SSP boundary calculated in Eq. (B5), and $B(\mu, \Delta_2)$ is real solutions of the following equation:

$$B^2\{(810\,000 - 86\,700\Delta_2\mu^2 + 83\,521\mu^4) + 810\,000B^2 + 270\,000B^4 + 30\,000B^6\} = 260\,100\Delta_2\mu^2. \tag{B15}$$

Considering that the left-hand side of Eq. (B15) is an even function which has a minimum equal to zero at $B = 0$ and a monotonically increasing function when $B > 0$, Eq. (B15) has only two real solutions with opposite signs which converge continuously to zero in the limit $\Delta_2 = 0$. Hence, we find that the bifurcation from NM to SSP is a pitchfork bifurcation for both uniaxial and biaxial cases.

2. Linear stability analysis of SSS

Using the SSS solutions $\tilde{v} = (0, 0, \tilde{v}_s)$ and $\tilde{\omega} = (0, 0, \tilde{\omega}_s)$, we obtain the following Jacobian J_{SSS} of the SSS solutions:

$$J_{\text{SSS}} = \begin{bmatrix} \gamma + a_1 q_1 - \tilde{v}_s^2 & -(a_2 - 1)\tilde{\omega}_s & 0 & \mu^{\text{iso}} + \mu q_1 & (a_2 - 1)\tilde{v}_s & 0 \\ (a_2 - 1)\tilde{\omega}_s & \gamma + a_1 q_2 - \tilde{v}_s^2 & 0 & -(a_2 - 1)\tilde{v}_s & \mu^{\text{iso}} + \mu q_2 & 0 \\ 0 & 0 & \gamma + a_1 q_3 - 3\tilde{v}_s^2 & 0 & 0 & \mu^{\text{iso}} + \mu q_3 \\ \nu^{\text{iso}} + \nu q_1 & b_2(q_2 - q_3)\tilde{v}_s & 0 & \zeta + b_1 q_1 - \tilde{\omega}_s^2 & 0 & 0 \\ b_2(q_3 - q_1)\tilde{v}_s & \nu^{\text{iso}} + \nu q_2 & 0 & 0 & \zeta + b_1 q_2 - \tilde{\omega}_s^2 & 0 \\ 0 & 0 & \nu^{\text{iso}} + \nu q_3 & 0 & 0 & \zeta + b_1 q_3 - 3\tilde{\omega}_s^2 \end{bmatrix}. \tag{B16}$$
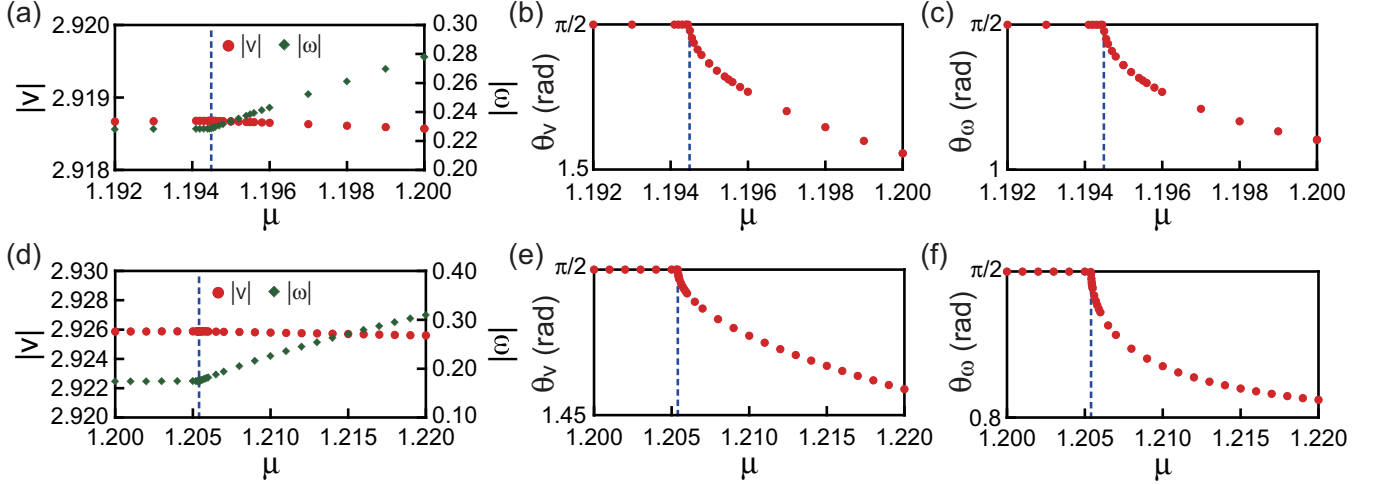
FIG. 9. Absolute values of velocity $\boldsymbol{v}$ and angular velocity $\boldsymbol{\omega}$, and the angles θ_v and θ_ω defined in the main text as a function of μ with a fixed value of $\gamma = 8.0$ for both uniaxial [(a)–(c)] and biaxial cases [(d)–(f)], respectively. The values of μ are changed around the bifurcation points from SSS to H, while the other parameters are the same as those used in the phase diagram in Fig. 2. The dashed vertical lines indicate the bifurcation points calculated using the method discussed in the main text.

Since it is readily verified that the degrees of the freedom in the z axis span the stable manifold, we considered the following Jacobian J'_{SSS} by removing the degrees of the freedom in the z axis from J_{SSS}:

$$J'_{\text{SSS}} = \begin{bmatrix} \gamma + a_1 q_1 - \tilde{v}_s^2 & -(a_2 - 1)\tilde{\omega}_s & \mu^{\text{iso}} + \mu q_1 & (a_2 - 1)\tilde{v}_s \\ (a_2 - 1)\tilde{\omega}_s & \gamma + a_1 q_2 - \tilde{v}_s^2 & -(a_2 - 1)\tilde{v}_s & \mu^{\text{iso}} + \mu q_2 \\ \nu^{\text{iso}} + \nu q_1 & b_2(q_2 - q_3)\tilde{v}_s & \zeta + b_1 q_1 - \tilde{\omega}_s^2 & 0 \\ b_2(q_3 - q_1)\tilde{v}_s & \nu^{\text{iso}} + \nu q_2 & 0 & \zeta + b_1 q_2 - \tilde{\omega}_s^2 \end{bmatrix}. \tag{B17}$$

Next, we define the characteristic polynomial $f_{\text{s}}(\lambda)$ of J'_{SSS}. In the biaxial case, substituting one of the nontrivial solutions of Eqs. (B6) and (B7) into $f_{\text{s}}(\lambda)$, we calculated the linear stability limit by numerically solving $f_{\text{s}}(0) = 0$ with respect to γ and μ. Here, the function ContourPlot on Mathematica was used. In the uniaxial case, J'_{SSS} always has a zero eigenvalue, and we obtain

$$f_{\text{s}}(\lambda) = \lambda \begin{vmatrix} -(\mu^{\text{iso}} + q_2\mu)\frac{\tilde{\omega}_s}{\tilde{v}_s} + a_1(q_1 - q_2) - \lambda & -(a_2 - 1)\tilde{\omega}_s & \mu^{\text{iso}} + \mu q_1 \\ (a_2 - 1)\tilde{\omega}_s - b_2(q_2 - q_1)\frac{\tilde{v}_s^2}{\tilde{\omega}_s} & -(\mu^{\text{iso}} + q_2\mu)\left(\frac{\tilde{\omega}_s}{\tilde{v}_s} + \frac{\tilde{v}_s}{\tilde{\omega}_s}\right) - \lambda & -(a_2 - 1)\tilde{v}_s \\ \mu^{\text{iso}} + \mu q_1 & 0 & -\frac{\tilde{v}_s}{\tilde{\omega}_s}(\mu^{\text{iso}} + q_2\mu) + b_1(q_1 - q_2) - \lambda \end{vmatrix}. \tag{B18}$$

Here we used the uniaxiality $q_2 = q_3$, Eqs. (B3) and (B4), and the following relations obtained from Eqs. (B6) and (B7):

$$(\mu^{\text{iso}} + q_3\mu)\frac{\tilde{\omega}_s}{\tilde{v}_s} = \tilde{v}_s^2 - (\gamma + a_1 q_3), \tag{B19}$$

$$(\nu^{\text{iso}} + q_3\nu)\frac{\tilde{v}_s}{\tilde{\omega}_s} = \tilde{\omega}_s^2 - (\zeta + b_1 q_3). \tag{B20}$$

Equating the determinant in Eq. (B18) to zero and setting $\lambda = 0$, we calculated the linear stability limit in the same way as performed in the biaxial case. As a result, we found that zero-eigenvalue bifurcations occur at the boundaries in both uniaxial $P = 0$ and biaxial case $P = 0.1$. Here zero-eigenvalue bifurcation means a bifurcation in which a real eigenvalue passes through 0.

Now we investigate the type of zero-eigenvalue bifurcation from SSS to H. To this end, we numerically calculated $|\boldsymbol{v}|, |\boldsymbol{\omega}|$, an angle θ_v between $\boldsymbol{v}$ and $\boldsymbol{a}$, and an angle θ_ω between $\boldsymbol{\omega}$ and

$\boldsymbol{a}$ by changing μ with a fixed $\gamma = 8.0$ for both uniaxial and biaxial cases in the phase diagrams in Fig. 2, respectively. Here both θ_v and θ_ω are equal to $\pi/2$ in SSS, while either θ_v or θ_ω deviates from $\pi/2$ in H. Figure 9 shows that $|\boldsymbol{v}|, |\boldsymbol{\omega}|, \theta_v$ and θ_ω are continuous at the bifurcation point. Hence, we find that $\boldsymbol{v}$ and $\boldsymbol{\omega}$ are also continuous at the bifurcation point. Furthermore, in the particle frame, if a H solution is $\tilde{\boldsymbol{v}} = (\tilde{v}_x, \tilde{v}_y, \tilde{v}_z)$ and $\tilde{\boldsymbol{\omega}} = (\tilde{\omega}_x, \tilde{\omega}_y, \tilde{\omega}_z)$, then $\tilde{\boldsymbol{v}} = (-\tilde{v}_x, -\tilde{v}_y, \tilde{v}_z)$ and $\tilde{\boldsymbol{\omega}} = (-\tilde{\omega}_x, -\tilde{\omega}_y, \tilde{\omega}_z)$ is also a H solution, since these symmetric solutions with respect to the z axis represent equivalent helical motions which appear with the same probability. These facts indicate that the bifurcations from SSS to H are pitchfork bifurcations.

3. Linear stability analysis of SSP

Using the SSP solutions $\tilde{\boldsymbol{v}} = (\tilde{v}_p, 0, 0)$ and $\tilde{\boldsymbol{\omega}} = (\tilde{\omega}_p, 0, 0)$, we obtain the following Jacobian J_{SSP} of the
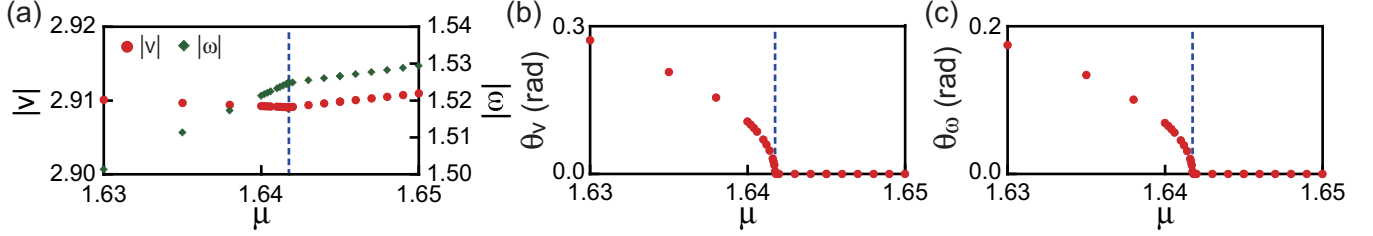
FIG. 10. Absolute values of velocity v and angular velocity ω, and the angles θ_v and θ_ω defined in the main text as a function of μ with a fixed value of $\gamma = 8.0$ for a biaxial case. The values of μ are changed around the bifurcation point from SSP to H, while the other parameters are the same as those used in the phase diagram in Fig. 2. The dashed vertical lines indicate the bifurcation points calculated using the method discussed in the main text.

SSP solutions:

$$J_{\mathrm{SSP}} = \begin{bmatrix} \gamma + a_1q_1 - 3\tilde{v}_p^2 & 0 & 0 & \mu^{\mathrm{iso}} + \mu q_1 & 0 & 0 \\ 0 & \gamma + a_1q_2 - \tilde{v}_p^2 & -(a_2-1)\tilde{\omega}_p & 0 & \mu^{\mathrm{iso}} + \mu q_2 & (a_2-1)\tilde{v}_p \\ 0 & (a_2-1)\tilde{\omega}_p & \gamma + a_1q_3 - \tilde{v}_p^2 & 0 & -(a_2-1)\tilde{v}_p & \mu^{\mathrm{iso}} + \mu q_3 \\ \nu^{\mathrm{iso}} + \nu q_1 & 0 & 0 & \zeta + b_1q_1 - 3\tilde{\omega}_p^2 & 0 & 0 \\ 0 & \nu^{\mathrm{iso}} + \nu q_2 & b_2(q_3-q_1)\tilde{v}_p & 0 & \zeta + b_1q_2 - \tilde{\omega}_p^2 & 0 \\ 0 & b_2(q_1-q_2)\tilde{v}_p & \nu^{\mathrm{iso}} + \nu q_3 & 0 & 0 & \zeta + b_1q_3 - \tilde{\omega}_p^2 \end{bmatrix}. \quad (\mathrm{B21})$$

Here $\tilde{v} = (\tilde{v}_p,0,0), \tilde{\omega} = (\tilde{\omega}_p,0,0)$ is a steady solution of Eqs. (A7) and (A8). Hence, $(\tilde{v}_p, \tilde{\omega}_p)$ is a nontrivial solution of the following equations:

$$(\mu^{\mathrm{iso}} + q_1\mu)\tilde{\omega}_p = \tilde{v}_p^3 - (\gamma + a_1q_1)\tilde{v}_p, \quad (\mathrm{B22})$$

$$(\nu^{\mathrm{iso}} + q_1\nu)\tilde{v}_p = \tilde{\omega}_p^3 - (\zeta + b_1q_1)\tilde{\omega}_p. \quad (\mathrm{B23})$$

Since it is readily verified that the degrees of the freedom in the x axis span the stable manifold, we considered the following Jacobian J'_{SSP} by removing the degrees of the freedom in the x axis from J_{SSS}:

$$J'_{\mathrm{SSP}} = \begin{bmatrix} \gamma + a_1q_2 - \tilde{v}_p^2 & -(a_2-1)\tilde{\omega}_p & \mu^{\mathrm{iso}} + \mu q_2 & (a_2-1)\tilde{v}_p \\ (a_2-1)\tilde{\omega}_p & \gamma + a_1q_3 - \tilde{v}_p^2 & -(a_2-1)\tilde{v}_p & \mu^{\mathrm{iso}} + \mu q_3 \\ \nu^{\mathrm{iso}} + \nu q_2 & b_2(q_3-q_1)\tilde{v}_p & \zeta + b_1q_2 - \tilde{\omega}_p^2 & 0 \\ b_2(q_1-q_2)\tilde{v}_p & \nu^{\mathrm{iso}} + \nu q_3 & 0 & \zeta + b_1q_3 - \tilde{\omega}_p^2 \end{bmatrix}. \quad (\mathrm{B24})$$

In our analysis, one of the nontrivial solutions of Eqs. (B22) and (B23) was substituted into J'_{SSP}. We calculated the largest eigenvalue of J'_{SSP} for each γ and μ, and plotted the linear stability limit as a contour on γ-μ space, where the real part of the largest eigenvalue $\lambda_{\max}$ equals to zero. Here the function ListContourPlot on Mathematica was used. By checking the imaginary part of the largest eigenvalues, we determined whether zero-eigenvalue bifurcation or Hopf bifurcation occurs at the boundaries. Consequently, the Hopf bifurcation occurs in the uniaxial case, while the zero-eigenvalue bifurcation occurs in the biaxial case $P = 0.1$.

Now we investigate the type of the zero-eigenvalue bifurcation from SSP to H in the biaxial case. To this end, we numerically calculated $|v|, |\omega|$, an angle θ_v between v and

a, and an angle θ_ω between ω and a by changing μ with a fixed $\gamma = 8.0$ for both uniaxial and biaxial cases in the phase diagrams in Fig. 2, respectively. Here both θ_v and θ_ω are equal to 0 in SSP, while either θ_v or θ_ω deviates from 0 in H. Figure 10 shows that $|v|, |\omega|, \theta_v$ and θ_ω are continuous at the bifurcation point. Hence, we find that v and ω are also continuous at the bifurcation point. Furthermore, in the particle frame, if a H solution is $\tilde{v} = (\tilde{v}_x, \tilde{v}_y, \tilde{v}_z)$ and $\tilde{\omega} = (\tilde{\omega}_x, \tilde{\omega}_y, \tilde{\omega}_z)$, then $\tilde{v} = (\tilde{v}_x, -\tilde{v}_y, -\tilde{v}_z)$ and $\tilde{\omega} = (\tilde{\omega}_x, -\tilde{\omega}_y, -\tilde{\omega}_z)$ is also a H solution, since these solutions which are symmetric with respect to the x axis represent equivalent helical motions which appear with the same probability. These facts indicate that the bifurcations from SSP to H are pitchfork bifurcations.

[1] K. Drescher, K. C. Leptos, I. Tuval, T. Ishikawa, T. J. Pedley, and R. E. Goldstein, Phys. Rev. Lett. **102**, 168101 (2009).

[2] A. P. Petroff, X.-L. Wu, and A. Libchaber, Phys. Rev. Lett. **114**, 158102 (2015).

[3] E. Lauga, W. R. DiLuzio, G. M. Whitesides, and H. A. Stone, Biophys. J. **90**, 400 (2006).

[4] J. Elgeti, U. B. Kaupp, and G. Gompper, Biophys. J. **99**, 1018 (2010).

[5] J. F. Jikeli, L. Alvarez, B. M. Friedrich, L. G. Wilson, R. Pascal, R. Colin, M. Pichlo, A. Rennhack, C. Brenker, and U. B. Kaupp, Nat. Commun. **6**, 7985 (2015).

[6] J. Gray, J. Exp. Biol. **32**, 775 (1955).

[7] H. Löwen, Eur. Phys. J. Special Topics **225**, 2319 (2016).

[8] F.-L. Wen, K.-t. Leung, and H.-Y. Chen, Phys. Rev. E **94**, 012401 (2016).

[9] F. Kümmel, B. ten Hagen, R. Wittkowski, I. Buttinoni, R. Eichhorn, G. Volpe, H. Löwen, and C. Bechinger, Phys. Rev. Lett. **110**, 198302 (2013).

[10] E. Tjhung, M. E. Cates, and D. Marenduzzo, Proc. Natl. Acad. Sci. USA **114**, 4631 (2017).

[11] T. Yamamoto and M. Sano, Soft Matter **13**, 3328 (2017).

[12] S. Herminghaus, C. C. Maass, C. Krüger, S. Thutupalli, L. Goehring, and C. Bahr, Soft Matter **10**, 7008 (2014).

[13] C. Krüger, G. Klös, C. Bahr, and C. C. Maass, Phys. Rev. Lett. **117**, 048003 (2016).

[14] C. C. Maass, C. Krüger, S. Herminghaus, and C. Bahr, Annu. Rev. Condens. Matter Phys. **7**, 171 (2016).

[15] W. F. Paxton, K. C. Kistler, C. C. Olmeda, A. Sen, S. K. St. Angelo, Y. Cao, T. E. Mallouk, P. E. Lammert, and V. H. Crespi, J. Am. Chem. Soc. **126**, 13424 (2004).

[16] H.-R. Jiang, N. Yoshinaga, and M. Sano, Phys. Rev. Lett. **105**, 268302 (2010).

[17] P. Romanczuk and L. Schimansky-Geier, Phys. Rev. Lett. **106**, 230601 (2011).

[18] M. Tarama and T. Ohta, J. Phys.: Condens. Matter **24**, 464129 (2012).

[19] M. Tarama and T. Ohta, Prog. Theor. Exp. Phys. **2013**, 013A01 (2013).

[20] S. Yabunaka, T. Ohta, and N. Yoshinaga, J. Chem. Phys. **136**, 074904 (2012).

[21] N. Yoshinaga, K. H. Nagai, Y. Sumino, and H. Kitahata, Phys. Rev. E **86**, 016108 (2012).

[22] P. G. de Gennes and J. Prost, *The Physics of Liquid Crystals*, 2nd ed. (Oxford University Press, Oxford, 1993).

[23] M. Ravnik and S. Žumer, Liq. Cryst. **36**, 1201 (2009).

[24] S. R. de Groot and P. Mazur, *Non-Equilibrium Thermodynamics* (Dover Publications, New York, 1984).

[25] T. Ohta and T. Ohkuma, Phys. Rev. Lett. **102**, 154101 (2009).

[26] H. Ebata and M. Sano, Sci. Rep. **5**, 8546 (2015).

[27] S. Chandrasekhar, *Liquid Crystals* (Cambridge University Press, Cambridge, 1977).

[28] J. R. Blake, J. Fluid Mech. **46**, 199 (1971).

[29] O. S. Pak and E. Lauga, J. Eng. Math. **88**, 1 (2014).

[30] K. Drescher, J. Dunkel, L. H. Cisneros, S. Ganguly, and R. E. Goldstein, Proc. Natl. Acad. Sci. USA **108**, 10940 (2011).

[31] E. Lauga and T. R. Powers, Rep. Prog. Phys. **72**, 096601 (2009).

[32] K. Drescher, R. E. Goldstein, N. Michel, M. Polin, and I. Tuval, Phys. Rev. Lett. **105**, 168101 (2010).

[33] T. Hiraiwa, K. Shitara, and T. Ohta, Soft Matter **7**, 3083 (2011).

[34] H. C. Crenshaw, Bull. Math. Biol. **55**, 197 (1993).

[35] R. N. Bearon, J. Math. Biol. **66**, 1341 (2013).

[36] M. Sandoval, Phys. Rev. E **87**, 032708 (2013).

[37] H. Larralde and F. Leyvraz, J. Phys. A: Math. Theor. **48**, 265001 (2015).

[38] F. J. Sevilla, Phys. Rev. E **94**, 062120 (2016).